

An iterative constraint energy minimizing generalized multiscale finite element method for contact problem

Zishang Li^{a,*}, Changqing Ye^a, Eric T. Chung^a

^a*Department of Mathematics, The Chinese University of Hong Kong, Shatin, Hong Kong SAR*

Abstract

This work presents an Iterative Constraint Energy Minimizing Generalized Multiscale Finite Element Method (ICEM-GMsFEM) for solving the contact problem with high contrast coefficients. The model problem can be characterized by a variational inequality, where we add a penalty term to convert this problem into a non-smooth and non-linear unconstrained minimizing problem. The characterization of the minimizer satisfies the variational form of a mixed Dirilect-Neumann-Robin boundary value problem. So we apply CEM-GMsFEM iteratively and introduce special boundary correctors along with multiscale spaces to achieve an optimal convergence rate. Numerical results are conducted for different highly heterogeneous permeability fields, validating the fast convergence of the CEM-GMsFEM iteration in handling the contact boundary and illustrating the stability of the proposed method with different sets of parameters. We also prove the fast convergence of the proposed iterative CEM-GMsFEM method and provide an error estimate of the multiscale solution under a mild assumption.

Keywords: multiscale finite element methods, high contrast problems, non-smooth boundary condition

1. Introduction

Composite materials have gained significant prominence in various industries and natural settings. The combination of different materials in composites allows for the creation of new materials with enhanced performance characteristics, making them highly sought after in fields such as aerospace, automotive, and construction, among others. Problems for composites arising from physics and engineering often exhibit multiple scales and high-contrast features. Traditional methods require very fine grids to solve those problems accurately, which leads to a great number of degrees of freedom and expensive computation. There have been many existing approaches in the literature to handle multiscale problems. These multiscale approaches include multiscale finite element methods [1, 2, 3, 4], heterogeneous multiscale methods [5, 6, 7], variational multiscale methods [8, 9], generalized finite element methods [10, 11], generalized multiscale finite element methods (GMsFEM) [12, 13, 14], and localized orthogonal decomposition methods [15, 16, 17, 18], etc. Most of these approaches are based on encoding fine-scale information

*Corresponding author.

Email address: zsl1@math.cuhk.edu.hk (Zishang Li)

into basis functions of finite element methods (FEMs), then solving original problems on multiscale finite element spaces whose dimensions have been greatly reduced compared to default FEMs. Many existing approaches in the field are focused on homogeneous or linear boundary value problems (BVPs) as model problems to study convergence theories and conduct numerical experiments. The extensions of those methods to non-smooth BVPs are relatively not easy to implement due to the presence of discontinuities, singularities, and other forms of non-smooth behavior in the solution or its derivatives. Given the high demand for solving non-smooth BVPs in practical applications, we will examine the effectiveness of current multiscale computational methods and further develop them to handle non-smooth mixed BVPs.

In many industrial applications or engineering problems, contact between deformable bodies plays a crucial role. The Signorini problem is a specific type of unilateral contact boundary value problem in partial differential equations that arises in the study of contact mechanics in solid mechanics. It was first published in the article [19] by Antonio Signorini. The solution to the Signorini problem led to the birth of the field of variational inequalities. They were introduced by Fichera in his analysis of the Signorini problem on the elastic equilibrium of a body under unilateral constraints [20]. In [21], Lions and Stampacchia extended Fichera's analysis to abstract variational inequalities associated with bilinear forms which are coercive or simply nonnegative in real Hilbert spaces as a tool for the study of partial differential elliptic and parabolic equations. Model reduction technique for solving standard PDE has been extended to variational inequality recently, where constructs the reduced basis by combining the greedy algorithm [22, 23] or the proper orthogonal decomposition methodology [24, 25]. Variational inequality can be characterized by a constrained minimization problem which also provides a numerical treatment [26]. Despite the fundamental role of contact in the mechanics of solids and structures, contact effects are rarely taken into account in structural analysis. Contact problems are inherently nonlinear [26]. So the modeling of contact phenomena poses serious difficulties in mathematics and computation. It is far more complex than that encountered in classical linear structural mechanics. In the field of computational contact mechanics, many studies have explored combining contact conditions with discrete formulations and algorithms [26, 27, 28, 29]. For instance, in [30], the authors revisited three different types of hybrid finite element methods for the Signorini problem. In [31], the authors used a hybrid variational formulation and applied the contact conditions to the displacement and the stress on the contact zone separately. Despite several previous studies and the rapid improvement in modern computer technology, most finite element software is not fully capable of solving contact problems with robust algorithms [32]. Hence there is still a challenge to design efficient and robust methods for computational contact problems.

The study and application of the Signorini problem have expanded beyond the physical or mechanical fields. For instance, in hydrostatics, consider a fluid contained in a porous domain Ω limited partly by a thin membrane Γ_C which is semi-permeable, meaning that it allows the fluid to pass through only in one direction to get in Ω [30]. In our work, we will focus on heterogeneous medium in mixed contact boundary problems. The representation of this model problem is provided in Fig. 1.

The main contribution of our work is as follows. We develop a new iterative multiscale method based on the CEM-GMsFEM for solving the Signorini problem. The variational inequality obtained from the Signorini problem can be characterized by a constrained minimizing problem, where the penalty method is a general technique by adding a penalty term to the objective function that penalizes violations of the constraints. Then it reduces to solving the unconstrained optimization problem by numerical methods. The construction of multiscale space starts with solving a local spectral problem in each coarse element, then the multiscale basis functions

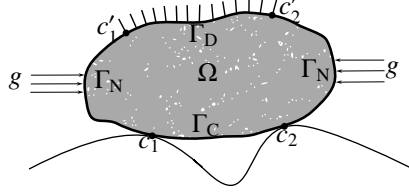


Figure 1: A deformable body in contact with a rigid obstacle.

are built by solving local constraint energy minimization problems in oversampling domains. The main difficulties in solving the problem arise from the nonlinearity of the contact conditions. Therefore, the semismooth Newton method is introduced during the construction of multiscale space. Specifically, we do not need to update all the basis during iterations, only those near the contact boundary. An analysis of the proposed method is presented. In particular, we show the convergence of our semismooth Newton iteration and give an error estimate. We present numerical results for two different heterogeneous permeability fields and verify that we can get accurate approximations with fewer degrees of freedom using the proposed method. The first case we consider contains small inclusions while the second one contains several high contrast channels. Both examples show our method works well to deal with the contact boundary and the iteration has fast convergence.

We begin, in the next section, by presenting the model of the Signorini problem and the preliminary treatment. Our iterative method and the framework of the multiscale method based on the CEM-GMsFEM are illustrated in Section 3. Then in section 4, we state the error analysis and show the convergence for our method. The numerical experiments are given in Section 5, where we also verify the effectiveness and efficiency of our method. Finally, some conclusions are provided in Section 6.

2. Preliminaries

2.1. Model problem

We will consider the contact problem of Signorini type for a second-order elliptic partial differential equation. We denote a Lipschitz domain by $\Omega \subset \mathbf{R}^d$ ($d = 2$ or 3), and $\kappa \in L^\infty(\Omega; \mathbf{R}^{d \times d})$ a matrix-valued function defined on Ω represents a heterogeneous permeability field with high contrast:

$$\begin{cases} -\operatorname{div}(\kappa \nabla u) = f & \text{in } \Omega, \\ u = 0 & \text{on } \Gamma_D, \\ \kappa \nabla u \cdot \mathbf{n} = p & \text{on } \Gamma_N, \\ u \leq 0, \quad \kappa \nabla u \cdot \mathbf{n} \leq 0, \quad (\kappa \nabla u \cdot \mathbf{n})u = 0 & \text{on } \Gamma_C, \end{cases} \quad (1)$$

where \mathbf{n} is the outward unit normal to $\partial\Omega$, Γ_D , Γ_N and Γ_C are three nonempty disjointed parts of $\partial\Omega$. In this paper, we present the following assumptions:

1. There exist two positive constants κ' and κ'' such that $0 < \kappa' \leq \kappa(\mathbf{x}) \leq \kappa'' < \infty$ for almost all $\mathbf{x} \in \Omega$.
2. The source term $f \in L^2(\Omega)$, and the inhomogenous Neumann boundary term $p \in L^2(\Gamma_N)$.

To solve this problem, it is appropriate to use a functional framework that involves a subset of the Sobolev space $H^1(\Omega)$ defined as

$$V := \{v \in H^1(\Omega) : v = 0 \text{ on } \Gamma_D\}.$$

The contact condition is then explicitly incorporated in the following closed convex set

$$K := \{v \in V : v \leq 0 \text{ on } \Gamma_C\}.$$

By the primal variational principle for the Signorini problem, the exact solution of the above contact problem (Eq. (1)) is characterized by the variational inequality: find $u \in K$ such that

$$a(u, v - u) \geq L(v - u), \quad \forall v \in K, \quad (2)$$

where

$$a(u, v) = \int_{\Omega} \kappa \nabla u \cdot \nabla v \, dx \text{ and } L(v) = \int_{\Omega} f v \, dx + \int_{\Gamma_N} p v \, d\sigma.$$

We introduce the notation for the energy norm $\|v\|_a := \sqrt{a(v, v)}$ on Ω . For a subdomain $\omega \subset \Omega$, we also introduce the norm $\|v\|_{a(\omega)} := \sqrt{\int_{\omega} \kappa \nabla u \cdot \nabla v \, dx}$.

By Theorem 3.9 (see [26]), the weak problem (Eq. (2)) is well-posed and the unique solution of this variational inequality exists. Moreover, this solution is also the minimizer of the constrained minimization problem: given the functional $F : V \rightarrow \mathbf{R}$ is of the form

$$F(v) = \frac{1}{2} a(v, v) - L(v),$$

find $u \in K$ such that

$$F(u) = \inf_{v \in K} F(v). \quad (3)$$

2.2. Penalty method

Constrained minimization problems involve optimizing functions subject to constraints and are generally more complex than unconstrained problems. Meanwhile, the unconstrained minimization problems have more well-established solving methods and find extensive applications in various industries and engineering fields, where they minimize a function without any constraints on the variables. So the primary objective of our research is to transform constrained minimization problems into unconstrained problems, and one commonly employed approach for achieving this conversion is the penalty method. The penalty method involves the introduction of additional penalty terms to the objective function, which effectively penalizes violations of the constraints. By incorporating these penalty terms, the original constrained problem is transformed into an unconstrained problem, allowing for the application of unconstrained optimization techniques and algorithms. Here, we introduce the penalty term $P : V \rightarrow \mathbf{R}$ and a new functional $F_{\varepsilon} : V \rightarrow \mathbf{R}$ depending on a real parameter $\varepsilon > 0$, of the form

$$F_{\varepsilon}(v) = F(v) + \frac{1}{\varepsilon} P(v).$$

Hence, in accordance with Theorem 3.1 in [26], for each $\varepsilon > 0$ there exists a $u_{\varepsilon} \in V$ which minimizes F_{ε} . The corresponding constrained minimization problem is: find $u_{\varepsilon} \in V$ such that

$$F_{\varepsilon}(u_{\varepsilon}) = \inf_{v \in V} F_{\varepsilon}(v). \quad (4)$$

Moreover, if the functionals F and P are Gateaux-differentiable, the minimizer u_ε can be characterized by

$$\langle DF(u_\varepsilon), v \rangle + \frac{1}{\varepsilon} \langle DP(u_\varepsilon), v \rangle = 0,$$

where $\langle \cdot, \cdot \rangle$ is the functional dual on V . To apply the penalty method to the Signorini condition, the penalty functional $P : V \rightarrow \mathbf{R}$ is taken as

$$P(v) = \frac{1}{2} \int_{\Gamma_C} v_+^2 d\sigma,$$

which satisfies a property: the more a candidate minimizer $v \in V$ violates the constraint $v \leq 0$ on the contact boundary Γ_C , the greater the penalty that must be paid. This functional P is also Gateaux-differentiable on V and

$$\begin{aligned} \langle DP(u), v \rangle &= \lim_{t \rightarrow 0} \frac{P(u + tv) - P(u)}{t} \\ &= \lim_{t \rightarrow 0^+} \frac{1}{2t} \int_{\Gamma_C} (u + tv)_+^2 - u_+^2 d\sigma \\ &= \lim_{t \rightarrow 0^+} \frac{1}{2t} \int_{\Gamma_C} \int_0^1 \frac{d}{ds} (u + stv)_+^2 ds d\sigma \\ &= \lim_{t \rightarrow 0^+} \frac{1}{2t} \int_{\Gamma_C} \int_0^1 2(u + stv)_+ tv ds d\sigma \\ &= \int_{\Gamma_C} u_+ v d\sigma. \end{aligned}$$

Thus, the characterization of the minimizer of the unconstrained minimization problem is: find $u_\varepsilon \in V$, such that

$$a(u_\varepsilon, v) + \frac{1}{\varepsilon} \int_{\Gamma_C} (u_\varepsilon)_+ v d\sigma = L(v), \quad \forall v \in V. \quad (5)$$

2.3. Semismooth Newton Method

To find the minimizer of the unconstrained minimization problem, we take the residual functional for the characterization Eq. (5) as

$$R(u) = a(u, v) + \frac{1}{\varepsilon} \int_{\Gamma_C} g(u)v d\sigma - L(v), \quad (6)$$

where we denote $g(u) = u_+ = \max\{0, u\}$. Then we need to find the root $u_\varepsilon \in V$, such that $R(u_\varepsilon) = 0$. Since $R(u)$ lacks the necessary differentiability in the classical sense, we must turn to generalized Newton methods for this nonlinear problem. One such generalized method is the semismooth Newton method. The definition of semismooth is cumbersome to handle [33]. To simplify, we introduce the following theorem which provides equivalent characterizations to our case.

Theorem 2.1. *Let $R : V \rightarrow \mathbf{R}$. Then, for $u \in V$, the following statements are equivalent:*

- (a) R is semismooth at u .
- (b) R is locally Lipschitz continuous at u , $R'(u; \cdot)$ exists, and for any $G \in \partial R(u + d)$,

$$\|Gd - R'(u, d)\| = O(\|d\|) \text{ as } d \rightarrow 0.$$

(c) R is locally Lipschitz continuous at u , $R'(u; \cdot)$ exists, and for any $G \in \partial R(u + d)$,

$$\|R(u + d) - R(u) - Gd\| = \mathcal{O}(\|d\|) \text{ as } d \rightarrow 0.$$

Here $R'(u; d)$ and $\partial R(u + d)$ are the directional derivative and collection of the generalized directional derivative of R at u in direction d respectively. The definition can be found in [33]. We find that $R(u)$ is semismooth on V . Then a generalized derivative is defined for the semismooth Newton procedure.

Definition 2.1. The mapping $R : V \rightarrow \mathbf{R}$ is Newton differentiable on the open set $U \subset V$, if there exists a family of mappings $G : U \rightarrow L(V, V')$ such that

$$\lim_{d \rightarrow 0} \frac{1}{\|d\|} \|R(u + d) - R(u) - G(u + d)d\| = 0.$$

for every $u \in U$. The operator G is referred to as Newton's derivative of R .

Note that $R(u)$ is Newton differentiable on V . The Newton derivative of $R(u)$ is

$$\langle G(u)d, v \rangle := a(d, v) + \frac{1}{\varepsilon} \int_{\Gamma_C} g'(u)dv \, d\sigma, \quad \forall d, v \in V,$$

where the derivative of $g(u)$ is

$$g'(u) = \mathbb{1}(u > 0) = \begin{cases} 1, & u > 0, \\ 0, & u \leq 0. \end{cases}$$

Similar to the classical Newton method, the semismooth Newton algorithm is stated in Algorithm 1:

Algorithm 1 Semismooth Newton method

Input: R, u_0, tol

- 1: R is Newton differentiable in $V, u_0 \in V, k = 0$
- 2: **while** $k < 1$ or $R(u_{k+1}) > \text{tol}$ **do**
- 3: Solve $G(u_k)d_k = R(u_k)$ to obtain d_k
- 4: $u_{k+1} = u_k - d_k, k = k + 1$
- 5: **end while**
- 6: **return** u_{k+1}

Output: the numerical solution u_{k+1}

The main procedure in variational form is: find u_k , such that

$$\begin{cases} a(d_k, v) + \frac{1}{\varepsilon} \int_{\Gamma_C} g'(u_k)d_k v \, d\sigma = a(u_k, v) + \frac{1}{\varepsilon} \int_{\Gamma_C} g(u_k)v \, d\sigma - L(v), \quad \forall v \in V, \\ u_{k+1} = u_k - d_k. \end{cases} \quad (7)$$

3. Numerical Method

3.1. Conversion of the contact problem

Although many theoretical derivations and problem transformations have been done for the Signorini contact problem. We still need to do some processing before using numerical methods and getting the numerical solution. The characterization of the minimizer of F_ε Eq. (5) in Section 2.2 can be considered as the weak form of the specific partial differential equation. Remarkably, it is identical with the weak form of the following Neumann boundary problem

$$\begin{cases} -\operatorname{div}(\kappa\nabla u) = f, & \text{in } \Omega, \\ u = 0, & \text{on } \Gamma_D, \\ \kappa\nabla u \cdot \mathbf{n} = p, & \text{on } \Gamma_N, \\ \kappa\nabla u \cdot \mathbf{n} = -\frac{1}{\varepsilon}g(u), & \text{on } \Gamma_C. \end{cases} \quad (8)$$

The weak formulation of Eq. (8) is to find $u \in V$ such that

$$a(u, v) = f(v) - \frac{1}{\varepsilon} \int_{\Gamma_C} u_{+,v} d\sigma + \int_{\Gamma_N} p v d\sigma, \quad \forall v \in V,$$

where

$$a(w, v) = \int_{\Omega} \kappa \nabla w \cdot \nabla v d\mathbf{x} \text{ and } f(v) = \int_{\Omega} f v d\mathbf{x}.$$

Consequently, it is possible that the numerical methods for solving Neumann boundary value problems can be applied to determine the contact problem minimizer.

To linearize the function $g(u)$, we can utilize the first-order Taylor series approximation. This approximation expresses $g(u)$ as follows:

$$g(u) \approx g(u_k) + g'(u_k)(u - u_k),$$

where $g'(u_k)$ represents the derivative of $g(u)$ evaluated at the point u_k . Thus, we have

$$\frac{1}{\varepsilon} g'(u_k) u + \kappa \nabla u \cdot \mathbf{n} = -\frac{1}{\varepsilon} [g(u_k) - g'(u_k) u_k].$$

Take b_k and q_k as

$$b_k = \frac{1}{\varepsilon} g'(u_k) \text{ and } q_k = -\frac{1}{\varepsilon} [g(u_k) - g'(u_k) u_k].$$

Then Eq. (8) can be converted into an inhomogeneous Robin boundary value problem

$$\begin{cases} -\operatorname{div}(\kappa\nabla u) = f, & \text{in } \Omega, \\ u = 0, & \text{on } \Gamma_D, \\ \kappa\nabla u \cdot \mathbf{n} = p, & \text{on } \Gamma_N, \\ b_k u + \kappa\nabla u \cdot \mathbf{n} = q_k, & \text{on } \Gamma_C. \end{cases} \quad (9)$$

We rewrite this mixed boundary problem Eq. (9) in a variational form

$$\int_{\Omega} \kappa \nabla u \cdot \nabla v d\mathbf{x} + \int_{\Gamma_C} b_k u v d\sigma = \int_{\Omega} f v d\mathbf{x} + \int_{\Gamma_N} p v d\sigma + \int_{\Gamma_C} q_k v d\sigma,$$

and the bilinear form satisfies

$$\tilde{a}(w, v; b_k) = \int_{\Omega} \kappa \nabla w \cdot \nabla v \, d\mathbf{x} + \int_{\Gamma_C} b_k w v \, d\sigma = a(w, v) + \int_{\Gamma_C} b_k w v \, d\sigma.$$

Here we introduce a notation for the bilinear form $\tilde{a}(\cdot, \cdot; b)$:

$$\tilde{a}(w, v; b) := \int_{\Omega} \kappa \nabla w \cdot \nabla v \, d\mathbf{x} + \int_{\Gamma_C} b w v \, d\sigma.$$

Then we have

$$a(u, v) + \frac{1}{\varepsilon} \int_{\Gamma_C} g'(u_k) u v \, d\sigma = \int_{\Omega} f v \, d\mathbf{x} + \int_{\Gamma_N} p v \, d\sigma - \frac{1}{\varepsilon} \int_{\Gamma_C} [g(u_k) - g'(u_k) u_k] v \, d\sigma. \quad (10)$$

This variational equation is exactly equivalent to the Eq. (7) obtained by the semismooth Newton iteration in Section 2.3 if we take $u = u_k - d_k$. In the case of Signorini typed contact problem, the function $g(u) = (u)_+$. Then we have

$$b_k(u_k) = \frac{1}{\varepsilon} g'(u_k) = \frac{1}{\varepsilon} \mathbb{1}(u_k > 0)$$

and

$$\begin{aligned} q_k(u_k) &= -\frac{1}{\varepsilon} [g(u_k) - g'(u_k) u_k] \\ &= -\frac{1}{\varepsilon} [(u_k)_+ - \mathbb{1}(u_k > 0)(u_k)_+] \\ &= -\frac{1}{\varepsilon} [(u_k)_+ - (u_k)_+] \\ &= 0. \end{aligned}$$

Thus, the variational form Eq. (10) can be simplified as: find $u_{k+1} \in V$, such that

$$a(u_{k+1}, v) + \frac{1}{\varepsilon} \int_{\Gamma_C} u_{k+1} v \cdot \mathbb{1}(u_k > 0) \, d\sigma = \int_{\Omega} f v \, d\mathbf{x} + \int_{\Gamma_N} p v \, d\sigma, \quad \forall v \in V. \quad (11)$$

By doing the iteration, we can obtain the minimizer of the unconstrained functional F_ε . Drawing upon the previous analysis, it is feasible to transform the contact problem into a mixed Robin boundary problem. This transformation holds significant importance as it may allow us to effectively handle this problem by modifying the established finite element tools and methodologies.

3.2. One step CEM-GMsFEM solver

We will focus on the numerical solution of the variational form Eq. (11) in one iteration by the CEM-GMsFEM method. Consider a conforming partition \mathcal{T}^H of a domain Ω into N finite elements K_i , where H denotes the coarse-mesh size. This is to be distinguished from another fine mesh \mathcal{T}^h with the mesh size h and will be utilized to compute multiscale basis functions. The fine element is represented as τ . For each coarse element $K_i \in \mathcal{T}^H$ with $1 \leq i \leq N$, we define an oversampling domain $K_i^m (m \geq 1)$ as the domain obtained by augmenting the coarse element K_i with an additional m layers of neighboring coarse elements. A representation of the fine grid, coarse grid, and oversampling domain is provided in Fig. 2. For this quadrilateral mesh, there

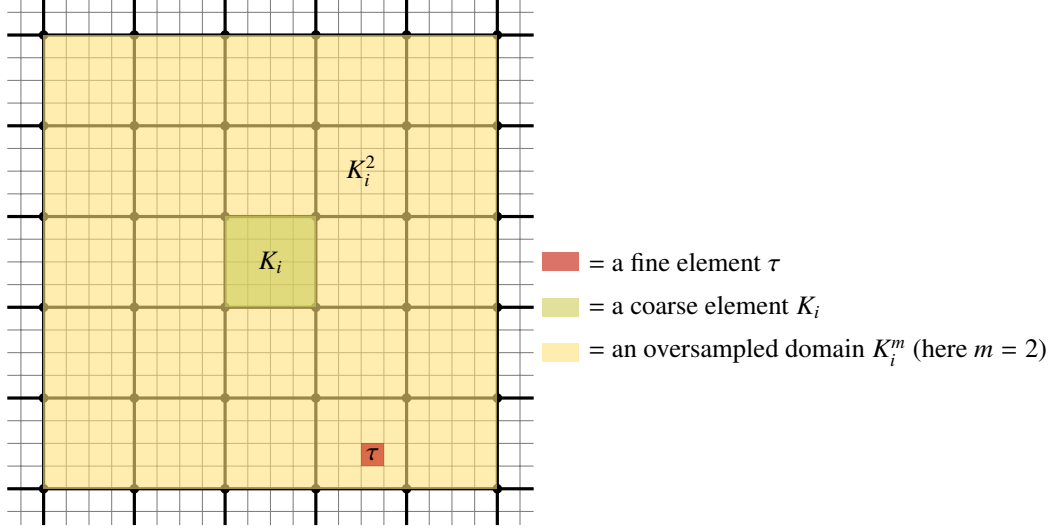


Figure 2: Illustration of meshes, fine element, coarse element, and oversampling domain.

are 4 vertices contained in an element. We can construct a set of Lagrange bases $\{\eta_i^1, \eta_i^2, \eta_i^3, \eta_i^4\}$ of the coarse element $K_i \in \mathcal{T}^H$. Then we define $\tilde{\kappa}(x)$ piecewise by

$$\tilde{\kappa}(x) = 3 \sum_{j=1}^4 \kappa(x) \nabla \eta_i^j \cdot \nabla \eta_i^j \quad (12)$$

in K_i which will be used in the following spectral problem.

The process of the construction of CEM-GMsFEM basis functions can be divided into two stages. The first stage involves the construction of the auxiliary space by solving a local spectral problem in each coarse element K_i : find eigen-pairs $\{\lambda_i^j, \phi_i^j\}$ such that

$$\tilde{a}_i(\phi_i^j, v; b) = \lambda_i^j s_i(\phi_i^j, v), \quad \forall v \in H^1(K_i). \quad (13)$$

where

$$\tilde{a}_i(u, v; b) = \int_{K_i} \kappa \nabla u \cdot \nabla v \, dx + \int_{\Gamma_{C \cap \partial K_i}} b u v \, d\sigma \quad \text{and} \quad s_i(u, v) = \int_{K_i} \tilde{\kappa} u v \, dx.$$

The bilinear form $s(w, v) := \int_{\Omega} \tilde{\kappa} w v \, dx$, and note that $s(w, v)$ can be well-defined on $L^2(\Omega)$. Similarly, we denote the norm

$$\|v\|_s := \sqrt{s(v, v)} \quad \text{and} \quad \|v\|_{s(K_i)} := \sqrt{s_i(v, v)}.$$

Let the eigenvalues $\{\lambda_i^j\}_{j=1}^{\infty}$ be arranged in an ascending order, we notice that $\lambda_i^1 = 0$ always holds. We define the local auxiliary multiscale space V_i^{aux} by using the first l_i eigenfunctions

$$V_i^{\text{aux}} := \text{span}\{\phi_i^j : 1 \leq j \leq l_i\},$$

and the orthogonal projection $\pi_i : V(K_i) \rightarrow V_i^{\text{aux}}$ with respect to the inner product $s(\cdot, \cdot)$ is

$$\pi_i(v) := \sum_{j=1}^{l_i} \frac{s(\phi_i^j, v)}{s(\phi_i^j, \phi_i^j)} \phi_i^j.$$

Then the global auxiliary space V^{aux} is defined by using these local auxiliary spaces $V_i^{\text{aux}} = \oplus_{i=1}^N V_i^{\text{aux}}$, and the global projection is $\pi := \sum_{i=1}^N \pi_i$ accordingly.

In the second stage, the multiscale basis functions are formed by solving some local constraint energy minimization problems in oversampling domains K_i^m . Let

$$V(K_i^m) = \left\{ v \in H^1(K_i^m) : v = 0 \text{ on } \Gamma_D \cap \partial K_i^m \text{ or } \Omega \cap \partial K_i^m \right\},$$

for each oversampling domain K_i^m . Then, the multiscale basis functions are defined by

$$\psi_i^{j,m} = \operatorname{argmin} \left\{ \tilde{a}(\psi, \psi; b) + s(\pi\psi - \phi_i^j, \pi\psi - \phi_i^j) : \psi \in V(K_i^m) \right\}, \quad (14)$$

which is a relaxed version of the energy minimization problem [34]

$$\psi_i^{j,m} = \operatorname{argmin} \left\{ \tilde{a}(\psi, \psi; b) : \psi \in V(K_i^m), \pi\psi = \phi_i^j \right\}.$$

We note that Eq. (14) is equivalent to: find $\psi_i^{j,m}$ such that

$$\tilde{a}(\psi_i^{j,m}, v; b) + s(\pi\psi_i^{j,m}, \pi v) = s(\phi_i^j, \pi v), \quad \forall v \in V(K_i^m). \quad (15)$$

Then the CEM-GMsFEM multiscale finite element space is defined by

$$V_{\text{ms}}^m = \operatorname{span} \left\{ \psi_i^{j,m} : 1 \leq j \leq l_i, 1 \leq i \leq N \right\}.$$

Given that the error analysis theory of the original CEM-GMsFEM strongly relies on the existence of L^2 source term, we might consider introducing function $\mathcal{N}_i^m p$ by imitating the construction of multiscale bases. This approach aims to extend the applicability of the CEM-GMsFEM to cases where an L^2 source term is not readily available or suitable. The function $\mathcal{N}_i^m p$ is defined by solving the following local problem (Eq. (16)) in the oversampling domain K_i^m . We can see that the zero-extension of a function in $V(K_i^m)$ still belongs to V .

Denote this process in one iteration as the CEM-GMsFEM solver. The output numerical solution of this solver is $\mathcal{S}\{b(\hat{u}), \kappa, f, p\}$, where \hat{u} is the substitutable input function. When the input function \hat{u} is given, it is easy to compute $b(\hat{u})$. We will perform the following four steps to obtain the new multiscale numerical solution:

STEP 1 Find $\mathcal{N}_i^m p \in V(K_i^m)$ such that,

$$\tilde{a}(\mathcal{N}_i^m p, v; b(\hat{u})) + s(\pi\mathcal{N}_i^m p, \pi v) = \int_{\partial K_i \cap \Gamma_N} p v \, d\sigma, \quad \forall v \in V(K_i^m), \quad (16)$$

then obtain

$$\mathcal{N}^m p = \sum_{i=1}^N \mathcal{N}_i^m p.$$

STEP 2 Construct the auxiliary space V^{aux} by Eq. (13) and the multiscale function space V_{ms}^m by Eq. (15).

STEP 3 Solve $w^m \in V_{\text{ms}}^m$ such that for all $v \in V_{\text{ms}}^m$,

$$\tilde{a}(w^m, v; b(\hat{u})) = \int_{\Omega} f v \, dx + \int_{\Gamma_N} p v \, d\sigma - \tilde{a}(N^m p, v; b_k).$$

STEP 4 Construct the numerical solution to approximate the real solution as

$$\mathcal{S}\{b(\hat{u}), \kappa, f, p\} \approx w^m + N^m p.$$

3.3. Iterative CEM-GMsFEM Algorithm

The iterative CEM-GMsFEM method involves using the CEM-GMsFEM solver iteratively to solve the contact problem. For the following iteration, the Robin coefficient b and new numerical solution \mathcal{S} can be computed by inputting the obtained numerical solution which involves executing the procedures in Section 3.2 to derive the updated multiscale solution. The condition for iteration termination is set as the error between the numerical solutions u_{k-1}^{cem} and u_k^{cem} is less than or equal to the tolerance (TOL):

$$\|u_k^{\text{cem}} - u_{k-1}^{\text{cem}}\| \leq \text{tol}. \quad (17)$$

We will conduct iterations until it satisfies this termination condition. The proposed multiscale method is summarized as in Algorithm 2.

Algorithm 2 Iterative CEM-GMsFEM for contact problem

Input: coefficient κ , source term f , Neumann boundary term p , tol

1: $k = 0$

2: **while** $k < 1$ or $\|u_k^{\text{cem}} - u_{k-1}^{\text{cem}}\| > \text{tol}$ **do**

3: $k = k + 1$

4: Use CEM-GMsFEM solver $\mathcal{S}\{b(u_{k-1}^{\text{cem}}), \kappa, f, p\}$ to obtain u_k^{cem}

5: **end while**

6: **return** k and u_k^{cem}

Output: the iterative number k and the numerical solution u_k^{cem}

4. Numerical experiments

In this section, we will present some numerical experiments to demonstrate that the multiscale method proposed is effective in a high contrast coefficient setting. We set the domain $\Omega = (0, 1)^2$. The medium parameter κ has a 400×400 resolution and only takes two values. The matrix phase value is $\kappa_m = 1$ and the value in the channels and inclusions is $\kappa_I \gg \kappa_m$, as shown in Fig. 3. We define contrast ratios $\kappa_R := \kappa_I / \kappa_m$. For simplifying the implementation, we especially choose $\tilde{\kappa} = 24\kappa/H^2$ instead of the original definition in Eq. (12). Moreover, we always fix the

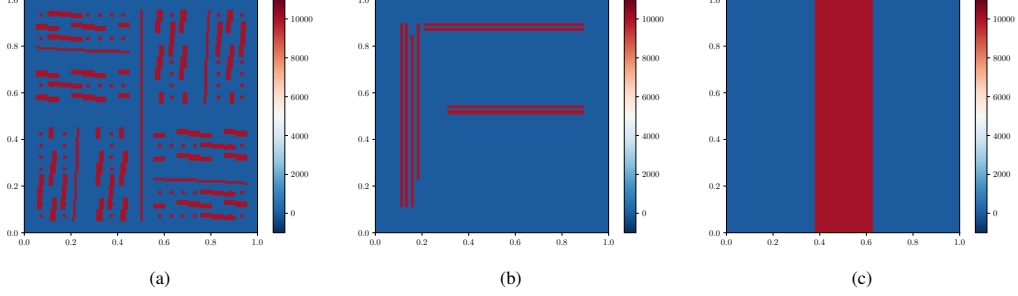


Figure 3: The permeability fields (a) medium A; (b) medium B; (c) medium C.

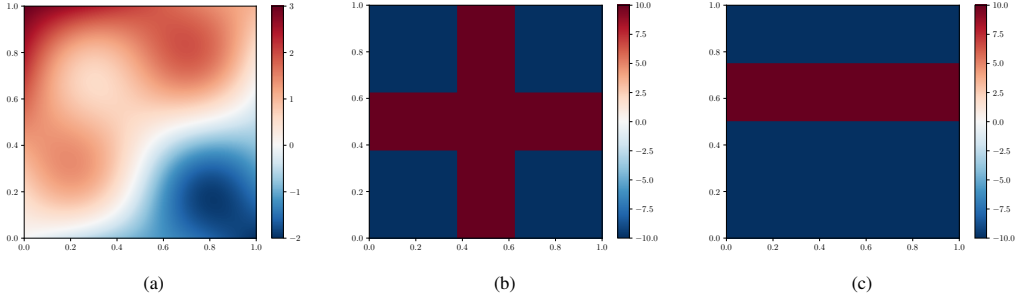


Figure 4: The source function (a) f_1 ; (b) f_2 ; (c) f_3 .

number of eigenvectors used to construct auxiliary space V_i^{aux} as l_m , i.e., $l_1 = l_2 = \dots = l_N = l_m$. The source functions f are given by $f_1(x, y) = -2x + 3y + \sin(2\pi x) \sin(2\pi y)$ for any $(x, y) \in \Omega$,

$$f_2 = \begin{cases} 10, & 0 < x < 1 \text{ and } \frac{3}{8} < y < \frac{5}{8}, \\ 10, & \frac{3}{8} < x < \frac{5}{8} \text{ and } 0 < y < 1, \\ -10, & \text{else,} \end{cases} \quad (18)$$

and

$$f_3 = \begin{cases} 10, & 0 < x < 1 \text{ and } \frac{1}{2} < y < \frac{3}{4}, \\ -10, & \text{else,} \end{cases} \quad (19)$$

in Fig. 4. The reference solutions u^{fe} are obtained by the bilinear Lagrange FEM with a fine mesh 400×400 . The default parameters are taken as follows: coarse mesh sizes $H = 1/80$, penalty parameter $\varepsilon = 10^{-4}$, contrast ratios $\kappa_R = 10^3$, eigenvector numbers $l_m = 4$ and oversampling layers $m = 4$.

After the k -th iteration, the numerical solution u_k^{cem} and the reference solution u_k^{fe} are obtained. To evaluate the efficiency of the multiscale method, we consider the relative L^2 error and energy error between u_k^{cem} and u_k^{fe} defined as

$$E_L^k := \frac{\|u_k^{\text{fe}} - u_k^{\text{cem}}\|_{L^2(\Omega)}}{\|u_k^{\text{fe}}\|_{L^2(\Omega)}} \text{ and } E_a^k := \frac{\|u_k^{\text{fe}} - u_k^{\text{cem}}\|_a}{\|u_k^{\text{fe}}\|_a},$$

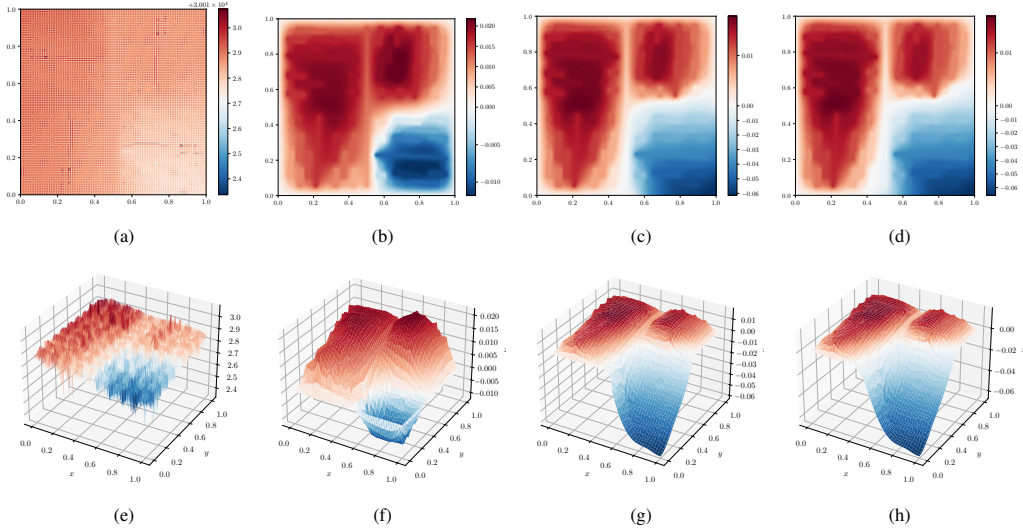


Figure 5: The solutions after iterations with medium A, using the source function f_1 and the initial value $u_0^{\text{cem}} = u_0^{\text{fe}} = u_0^0$. The first row shows the contour images, and the second row displays the 3D images. The iteration number: (a)(e) $k=1$; (b)(f) $k=2$; (c)(g) $k=3$; (d)(h) $k=8$.

and the iterative rate of u_{k-1}^{cem} and u_k^{cem} in two norms defined as

$$T_L^k := \frac{\|u_{k-1}^{\text{cem}} - u_k^{\text{cem}}\|_{L^2(\Omega)}}{\|u_{k-1}^{\text{cem}}\|_{L^2(\Omega)}} \quad \text{and} \quad T_a^k := \frac{\|u_{k-1}^{\text{cem}} - u_k^{\text{cem}}\|_a}{\|u_{k-1}^{\text{cem}}\|_a}.$$

4.1. Model problem 1

We begin with a more challenging model by applying contact boundary conditions to all boundaries $\partial\Omega$. While this might slightly different from the typical physics situation, our focus lies on the mathematical aspects and evaluating the effectiveness of our method with such nonlinear boundaries. The model problem is

$$\begin{cases} -\operatorname{div}(\kappa\nabla u) = f & \text{in } \Omega, \\ u \leq 0, \quad \kappa\nabla u \cdot \mathbf{n} \leq 0, \quad (\kappa\nabla u \cdot \mathbf{n})u = 0 & \text{on } \partial\Omega, \end{cases} \quad (20)$$

where κ is a highly heterogeneous permeability field generated from Fig. 3a and Fig. 3b, the source term f is taken as f_1 in the conducted experiments. Without loss of generality, the iteration processes are started with an initial value of $u_0^{\text{cem}} = u_0^{\text{fe}} = u_0^0 = 0$ in these two cases. To analyze the numerical results after iterations, we present contour images and 3D images respectively, see Fig. 5 and Fig. 6. With either of these two mediums, the results of the first numerical iteration oscillate, while after the second iteration, the values on the boundary converge to zero. Through a comparison of the outcomes from the iterations, it is apparent that the values of the contact boundaries have changed significantly, especially as the values decrease to less than or equal to zero. This result serves as an initial confirmation of the efficacy and accuracy of our methodology.

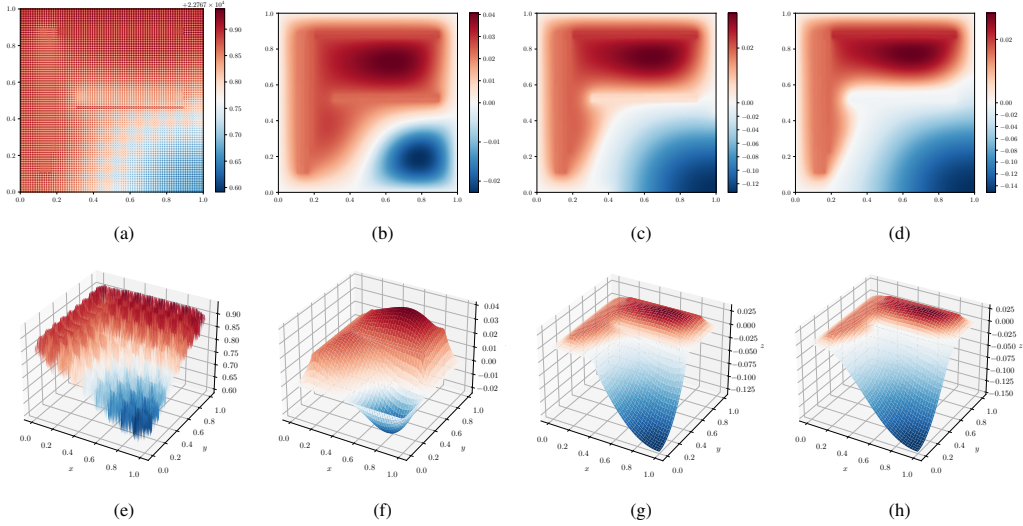


Figure 6: The solutions after iterations with medium B, using the source function f_1 and the initial value $u_0^{\text{cem}} = u_0^{\text{fe}} = u_0^0$. The first row shows the contour images, and the second row displays the 3D images. The iteration number: (a)(e) $k=1$; (b)(f) $k=2$; (c)(g) $k=3$; (d)(h) $k=8$.

4.2. Model problem 2

In this subsection, we consider the following mixed contact boundary problem,

$$\begin{cases} -\operatorname{div}(\kappa \nabla u) = f & \text{in } \Omega, \\ u = 0 & \text{on } \Gamma_D, \\ \kappa \nabla u \cdot \mathbf{n} = 0 & \text{on } \Gamma_N, \\ u \leq 0, \quad \kappa \nabla u \cdot \mathbf{n} \leq 0, \quad (\kappa \nabla u \cdot \mathbf{n})u = 0 & \text{on } \Gamma_C. \end{cases} \quad (21)$$

Let $\Gamma_D = [0, 1] \times \{1\}$, $\Gamma_C = [0, 1] \times \{0\}$, and $\Gamma_N = \partial\Omega \setminus (\Gamma_D \cup \Gamma_C)$.

4.2.1. For testing accuracy

To verify the effectiveness of our method for mixed contact boundary value problems, we consider highly heterogeneous permeability fields κ generated from Fig. 3a and Fig. 3b. The source term for these cases is denoted as f_2 . We initialize both iteration processes with $u_0^{\text{cem}} = u_0^{\text{fe}} = u_0^0$.

The Fig. 7 and Fig. 8 demonstrate that our proposed method effectively satisfies the conditions that the Dirichlet boundary values equal to 0 and the contact boundary values less than or equal to 0. Additionally, the results exhibit a rapid convergence rate when a suitable initial condition is utilized. These findings support the effectiveness of our method in handling the nonlinear and non-smooth conditions in the mixed contact boundary problem.

4.2.2. For different initial guesses and parameters

To study the impact of various initial conditions, we set two more initial conditions with different power numbers on the results of numerical solution: $u_0^1 = -x - y$ and $u_0^2 = -x^2/2 - y^2/2$. Also, we want to evaluate the impact of parameters on the results of solving nonlinear contact

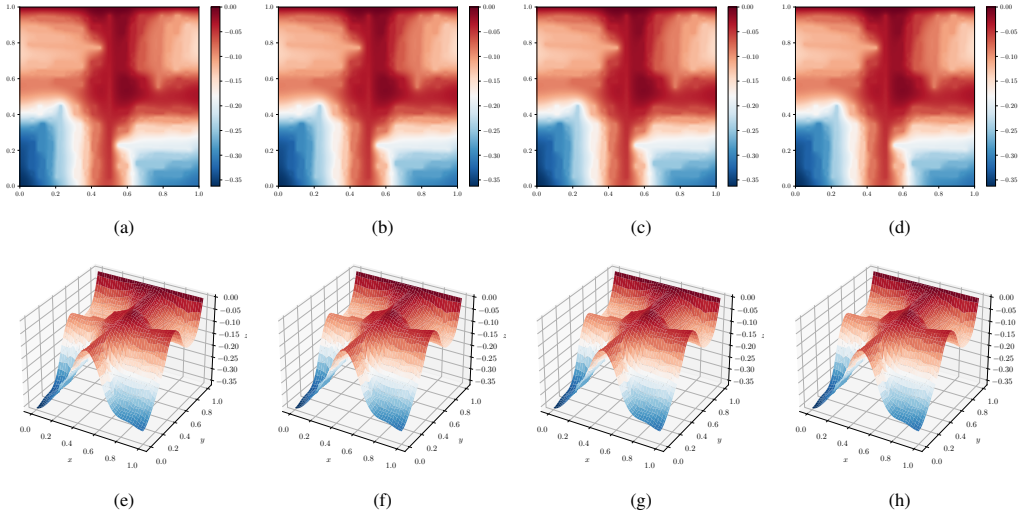


Figure 7: The solutions after iterations with medium A, using the source function f_2 and the initial value $u_0^{\text{cem}} = u_0^{\text{fe}} = u_0^0$. The first row shows the contour images, and the second row displays the 3D images. The iteration number: (a)(e) $k=1$; (b)(f) $k=2$; (c)(g) $k=3$; (d)(h) $k=8$.

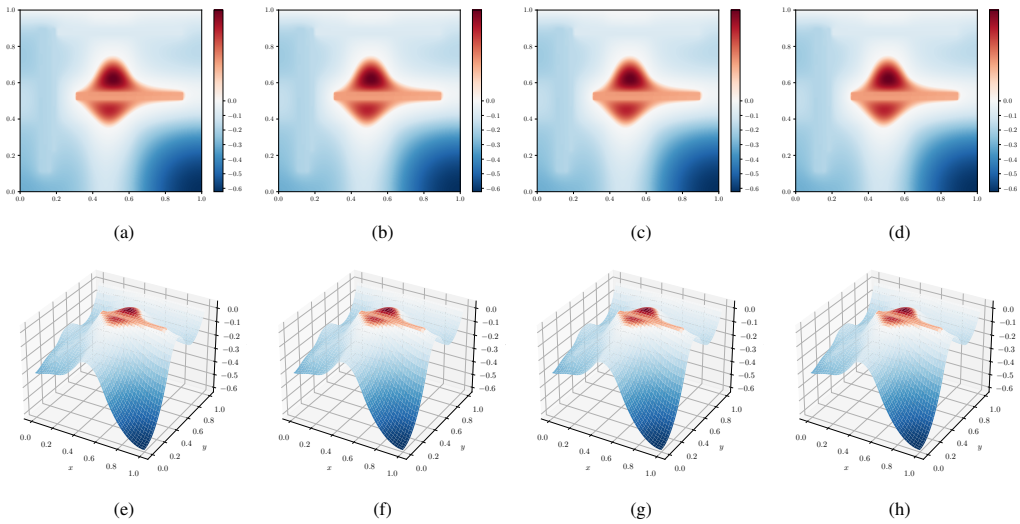


Figure 8: The solutions after iterations with medium B, using the source function f_2 and the initial value $u_0^{\text{cem}} = u_0^{\text{fe}} = u_0^0$. The first row shows the contour images, and the second row displays the 3D images. The iteration number: (a)(e) $k=1$; (b)(f) $k=2$; (c)(g) $k=3$; (d)(h) $k=8$.

boundary problems. We select several sets of parameters and test the variation of the relative error and the iteration rate with several iterations under these different parameter conditions. For these cases, the permeability field κ is highly heterogeneous and is generated from Fig. 3c. The source term is denoted as f_3 . Through several experiments, we seek to analyze the behavior of different parameters under various initial conditions throughout the iterations.

The numerical experimental results, as depicted in Fig. 9, Fig. 11 and Fig. 10, provide valuable insights into our analysis. According to the definition of the iteration rate, only when u_2^{cem} is solved, T_L and T_a can be calculated. Therefore, the plots start from $k = 2$. In Figs. 9a, 10a and 11a, the initial condition $u_0^{\text{cem}} = u_0^{\text{fe}} = u_0^0$ is considered, and it shows the error and iterative rate. Similarly, Figs. 9b, 10b and 11b, as well as Figs. 9c, 10c and 11c illustrate the results with different initial conditions: $u_0^{\text{cem}} = u_0^{\text{fe}} = u_0^1$ and $u_0^{\text{cem}} = u_0^{\text{fe}} = u_0^2$, respectively. By comparing the three subplots in each figure, we observe that different initial conditions do not significantly affect the numerical solution obtained through the iterative process in this model setting.

The results indicate that as the number of iterations increases, the relative error remains consistently small, indicating that the difference between the solution obtained via our proposed method and the finite element solution is tiny. The relative error between the solutions obtained using our method and the Finite Element Method in the energy norm exhibits a similar trend to that in the L^2 norm, with the error in the energy norm consistently greater than that in the L^2 norm. The iterative rates keep being small. The consistent small iterative rates indicate that good convergence results are achieved after the first iteration in this model setting. The impact of further numerical iterations on the results is minimal, emphasizing our method is powerful. The numerical results demonstrate that our method achieves small errors and fast convergence rates across various sets of different parameters. However, different parameter settings still have some impact on the results.

In Fig. 9, we investigate the influence of different coarse mesh sizes H , specifically $H = 1/20$, $H = 1/40$, $H = 1/80$, and $H = 1/100$. As expected, when $H = 1/20$, the errors between the numerical solutions and the finite element solutions are the largest. As the coarse mesh size decreases, the error also decreases. Additionally, we observe that the rate of iteration in the numerical solution increases as the coarse mesh size decreases. By using a smaller coarse mesh size, the numerical solution can capture more detailed features of the problem, leading to reduced errors and improved iteration rates. However, it is important to make a balance between mesh size and computational resources, as using excessively fine meshes may lead to increased computational costs.

The Fig. 10 analyzes the effects of different oversampling layers m , varying from 2 to 5. We can observe that as the number of oversampling layers increases, the performance improves. The additional oversampling layers allow for finer resolution in capturing the details of the problem, leading to a more accurate representation of the solution. Actually, the relative error of ($\kappa_R = 10^3$, $m = 3$) improves many times over ($\kappa_R = 10^3$, $m = 2$). Similarly, as emphasized in the experiment of convergence rate, the L^2 norm errors ($\approx 10^{-14}$) are constantly smaller than energy norm errors ($\approx 10^{-13}$). This phenomenon reveals the potential of the CEM-GMsFEM in discovering contact models of high contrast problems.

Lastly, Fig. 11 explores the impact of different eigenvector numbers l_m , ranging from 2 to 5. Generally, increasing the eigenvector number leads to better results in the numerical solution. However, we also observe that when $l_m = 3$ and $l_m = 4$, the relative error and iteration rates are very similar. This suggests that the influence of the eigenvector number on the results may be affected by other parameters, such as coarse mesh sizes H and oversampling layers m . Further analysis and experimentation are necessary to investigate the interactions between different pa-

parameters and their collective impact on the accuracy and convergence behavior of the numerical solution.

By examining these figures, we know how these parameters affect the accuracy and convergence of our method. This analysis allows us to select more suitable parameter settings for future experiments, thereby improving the overall performance of our approach.

4.2.3. For interdependent parameters

In this section, we examine how the numerical solution errors vary with two different parameters. The permeability fields κ are highly heterogeneous and are generated based on the data provided in Fig. 3a and Fig. 3b. The source term is taken as f_1 . Similar to previous experiments, we initiate the iteration process with $u_0^{\text{cem}} = u_0^{\text{fc}} = u_0^0$. Like previous experiment results in Section 4.2.2, the numerical results u_8^{cem} in this section remains stable to different parameters with very small error, therefore we consider it as the approximate solution u_∞^{cem} .

The results are reported in Fig. 12 and Fig. 13 for two different mediums. Notably, both sets of results sets of results have similar trends and characteristics. We will focus our analysis on the data of Fig. 12. We concentrate on investigating numerical errors by varying the coarse grids and oversampling layers, and then plot the results in Fig. 12a. An important observation is that errors will increase if we only reduce H while not enlarging oversampling layers m , which is distinct from traditional finite element methods. Then, focusing on $m = 2$, we can see that E_L and E_a grows like $O(H^{-1})$. Another observation is that when $m = 3$ and $m = 4$, the error caused by different H becomes very tiny. A finer coarse mesh requires a larger oversampling layer to obtain a smaller relative error. In Fig. 12b illustrates how coarse grid and basis number affect the numerical error. The utilization of a finer mesh and an increased number of basis functions yields a substantial reduction in error. Notably, when the number of basis functions 3, the relative error can be effectively constrained to below 5%. We test numerical errors with different contrast ratios κ_R and oversampling layers m , shown in Fig. 12c. It is not surprising that high contrast ratios will deteriorate numerical accuracy. Fortunately, the increase in oversampling layers m mitigates this deterioration. We then plot numerical error under different basis numbers and oversampling layers in Fig. 12d. It is observed that the relative error diminishes as the number of basis functions increases and the oversampling domain expands. When increasing the number of oversampling layers to $m = 4$ or $m = 5$, the relative error remains small, consistently staying below 10%. What's more, further increasing the basis number l_m does not lead to significant improvements in the numerical results. Therefore, to strike a balance between computational complexity and result accuracy, we can choose the parameter values $H = 1/80$, $m = 3$, and $l_m = 3$ for our experimental settings.

5. Analysis

Theorem 5.1. *Suppose that u_* is the real solution to the mixed contact boundary value problem Eq. (1). If $\|u_0 - u_*\|_a$ is sufficiently small, then the semismooth Newton iteration is well-defined and converges superlinearly to u_* .*

Proof. Since u_* is the real solution to the model problem Eq. (1), we have $R(u_*) = 0$. From Section 2.3, we know that the residual functional $R(u)$ in Eq. (6) is Newton differentiable on the open set $U \subset V$, and the derivative of $R(u)$ is

$$\langle G(u)w, v \rangle = a(w, v) + \frac{1}{\varepsilon} \int_{\Gamma_C} g'(u)wv \, d\sigma.$$

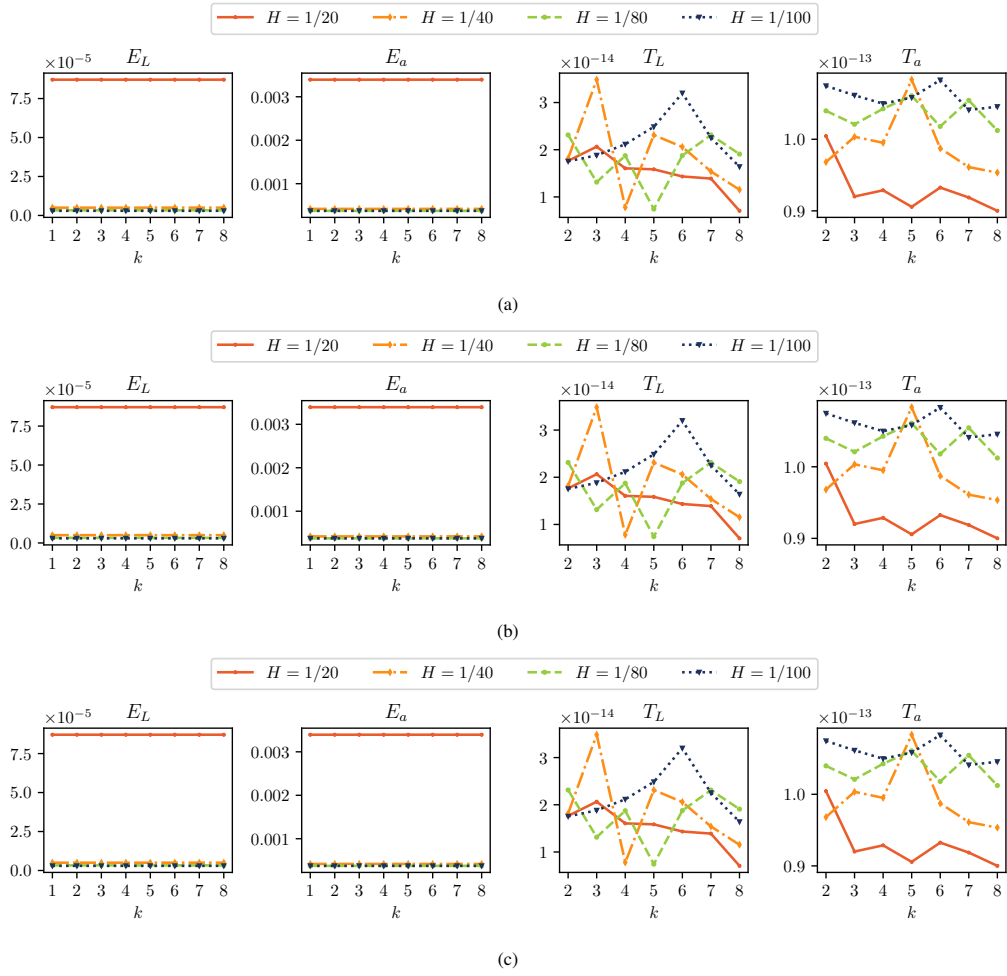


Figure 9: The relative error and iterative rate of solutions under different coarse mesh sizes H , with medium C, using the source function f_3 . The initial conditions: (a) $u_0^{\text{cem}} = u_0^{\text{fe}} = u_0^0$, (b) $u_0^{\text{cem}} = u_0^{\text{fe}} = u_0^1$, (c) $u_0^{\text{cem}} = u_0^{\text{fe}} = u_0^2$.

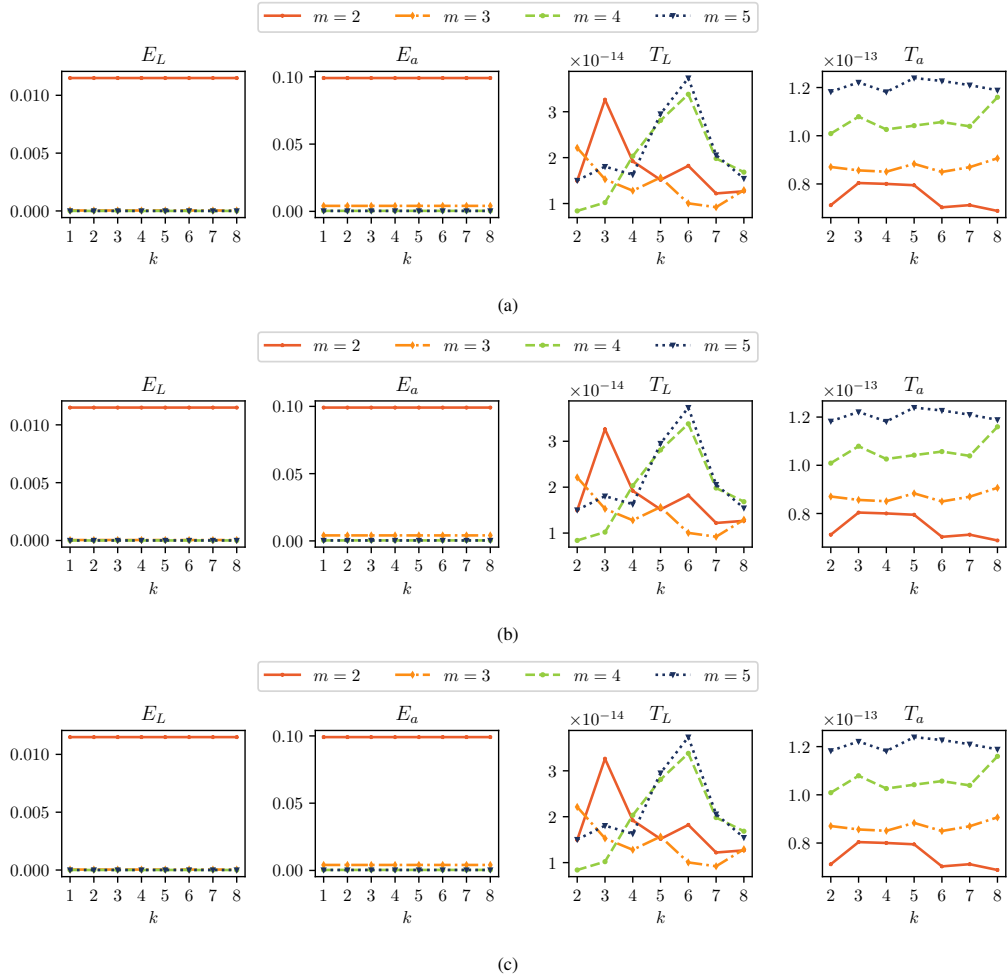


Figure 10: The relative error and iterative rate of solutions under different oversampling layers m , with medium C, using the source function f_3 . The initial conditions: (a) $u_0^{\text{cem}} = u_0^{\text{fe}} = u_0^0$, (b) $u_0^{\text{cem}} = u_0^{\text{fe}} = u_0^1$, (c) $u_0^{\text{cem}} = u_0^{\text{fe}} = u_0^2$.

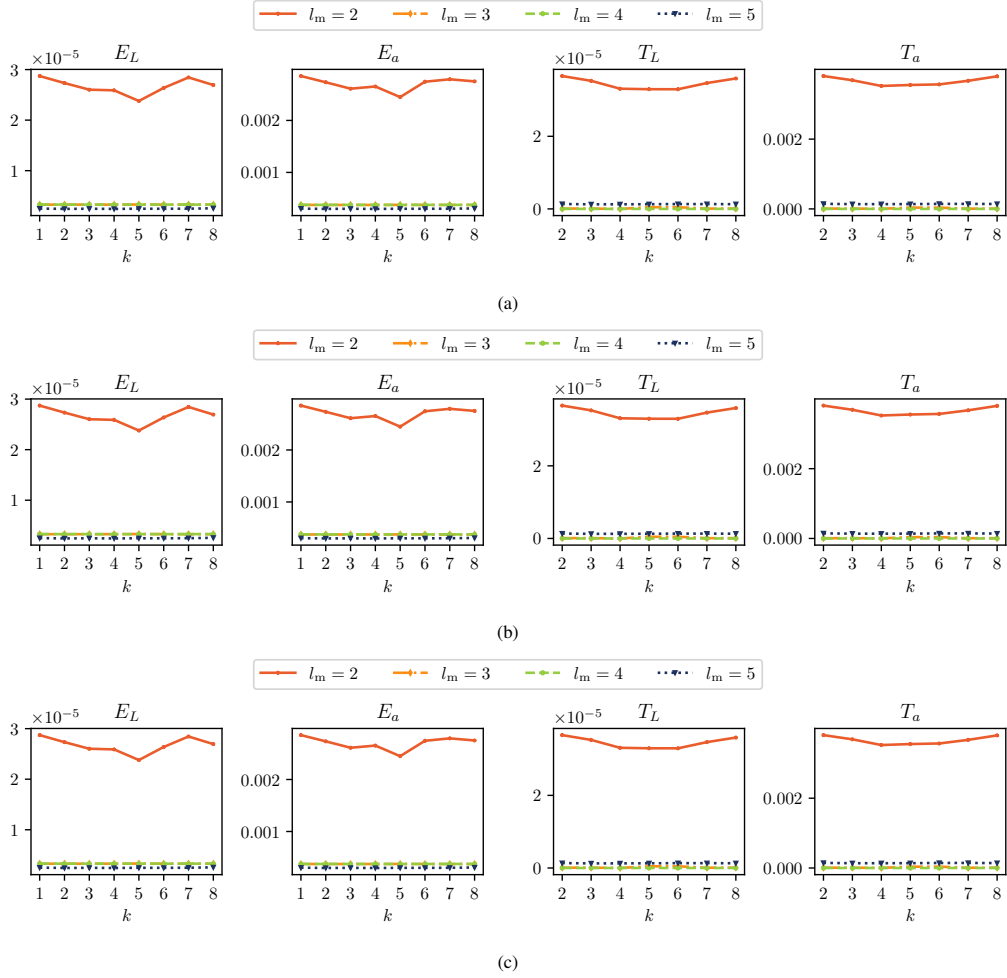
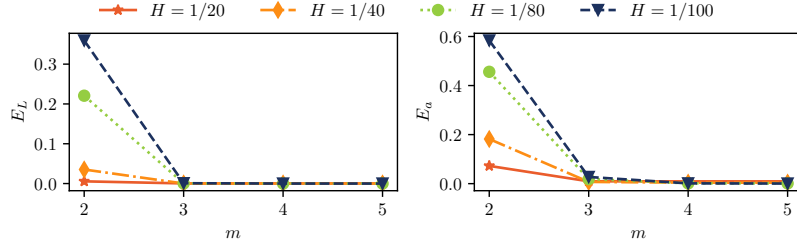
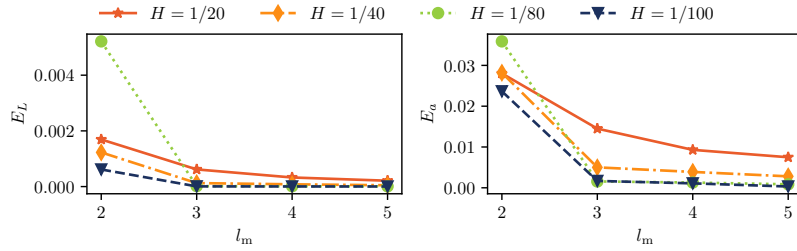


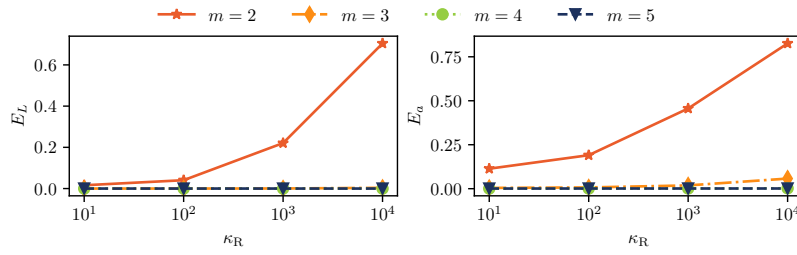
Figure 11: The relative error and iterative rate of solutions under different eigenvector numbers l_m , with medium C, using the source function f_3 . The initial conditions: (a) $u_0^{\text{cem}} = u_0^{\text{fe}} = u_0^0$, (b) $u_0^{\text{cem}} = u_0^{\text{fe}} = u_0^1$, (c) $u_0^{\text{cem}} = u_0^{\text{fe}} = u_0^2$.



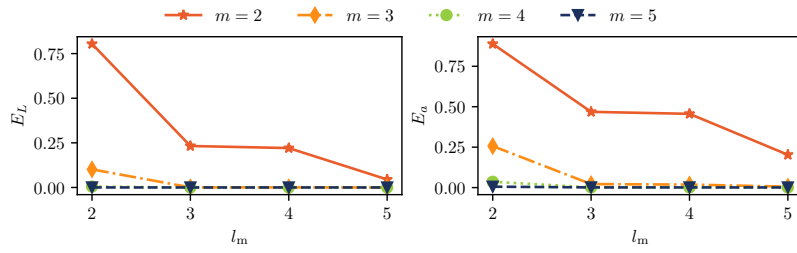
(a)



(b)

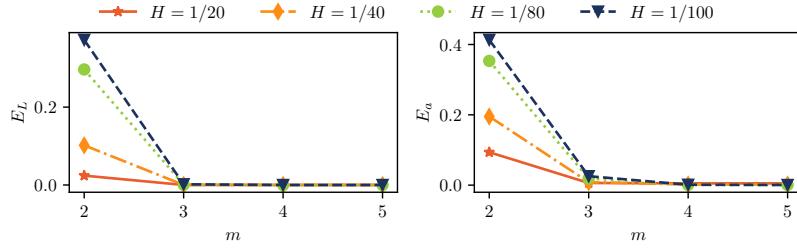


(c)

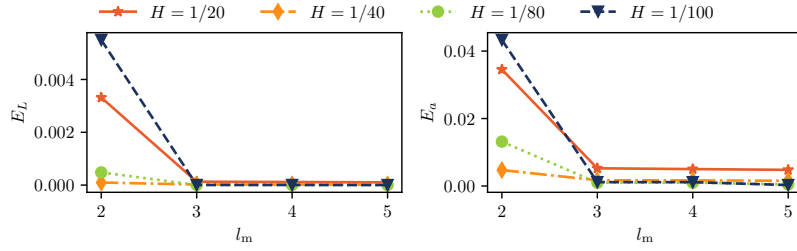


(d)

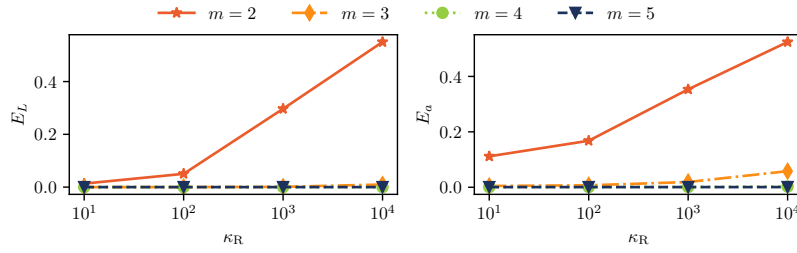
Figure 12: The relative errors in the energy and L^2 norm of numerical solutions with medium A, using the source function f_1 and the initial value $u_0^{\text{cem}} = u_0^{\text{fe}} = u_0^0$. (a) with different H and m ; (b) with different H and l_m ; (c) with different κ_R and m ; (d) with different l_m and m .



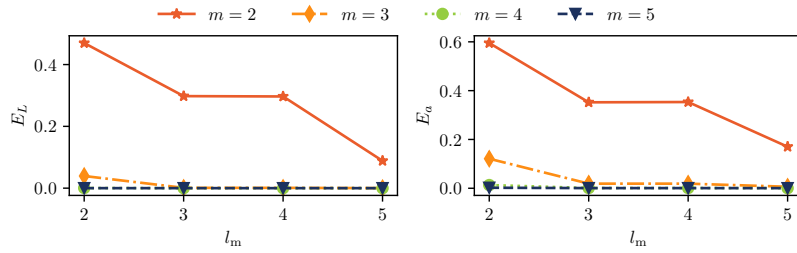
(a)



(b)



(c)



(d)

Figure 13: The relative errors in the energy and L^2 norm of numerical solutions with medium B, using the source function f_1 and the initial value $u_0^{\text{cem}} = u_0^{\text{ce}} = u_0^0$. (a) with different H and m ; (b) with different H and l_m ; (c) with different κ_R and m ; (d) with different l_m and m .

Since $\int_{\Gamma_C} g'(u)w^2 d\sigma \geq 0$, we have

$$\langle G(u)w, w \rangle \geq \|w\|_a^2.$$

Therefore, $G(u)$ is nonsingular for all $u \in U$ and $\{\|G(u)^{-1}\| : u \in U\}$ is bounded. From Theorem 3.2 in [33], the semismooth Newton method mentioned in Section 2.3 satisfies all conditions with the superlinear convergence to u_* if $\|u_0 - u_*\|_a$ is sufficiently small. \square

Lemma 5.2 (See [35]). *Let u be the exact solution to the variational form Eq. (11), $\mathcal{S}\{b(u), \kappa, f, p\}$ be the output numerical solution obtained in one iteration of CEM-GMsFEM solver with the input function u . Then*

$$\|\mathcal{S}\{b(u), \kappa, f, p\} - u\|_a \leq C'H (\|f\|_{L^2} + \|p\|_{L^2(\Gamma_N)}), \quad (22)$$

where H is the coarse mesh size, C' is a constant that does not explicitly depend on the penalty parameter ε or the contrast ratio κ_R under carefully selecting the numbers of oversampling layers m and eigenvector number l_m .

When considering two different input functions u' and u'' , the main distinction in the outputs of the CEM-GMsFEM solver $\mathcal{S}\{b(u'), \kappa, f, p\}$ and $\mathcal{S}\{b(u''), \kappa, f, p\}$ are observed only on the contact boundary Γ_C . Based on this, we may have the following assumption:

Assumption 5.3. For the output of one step CEM-GMsFEM solver $\mathcal{S}\{b, \kappa, f, p\}$, there exist positive constants r_0 and $C_* = 1 + \delta$ with $\delta > 0$, such that for all input functions u' and u'' belong to a neighbourhood $\mathcal{B}_{r_0}(u_*) \subset V$, the following inequality holds:

$$\|\mathcal{S}\{b(u'), \kappa, f, p\} - \mathcal{S}\{b(u''), \kappa, f, p\}\|_a \leq C_* \|u' - u''\|_a.$$

Theorem 5.4. *Under the Assumption 5.3, suppose $u_i, u_i^{\text{cem}} \in \mathcal{B}_{r_0}(u_*) \subset V$ for all $0 \leq i \leq k$ and $u_0 = u_0^{\text{cem}}$. Let u_{i+1} be the exact solution derived by Eq. (11), u_{i+1}^{cem} represent the numerical solution derived by Iterative CEM-GMsFEM Algorithm 2 iterated from u_i^{cem} , C' and C_* be the constants defined in Lemma 5.2 and Assumption 5.3 respectively. Then there exist constants M and k_0 such that for all $k \leq k_0$,*

$$\|u_{k+1} - u_{k+1}^{\text{cem}}\|_a \leq C'MH (\|f\|_{L^2} + \|p\|_{L^2(\Gamma_N)}), \quad (23)$$

where $k_0 = \lfloor \frac{\log(M\delta+1)}{\log(\delta+1)} - 1 \rfloor$. Furthermore, let r' be the convergence radius of semismooth Newton method and take $r := \min\{r_0, r'\}$. The following estimate holds:

$$\|u_* - u_{k+1}^{\text{cem}}\|_a < 2^{-(k+1)}r + C'MH (\|f\|_{L^2} + \|p\|_{L^2(\Gamma_N)}).$$

Proof. Let $\tilde{u}_{k+1}^{\text{cem}}$ represent the numerical solution obtained by Iterative CEM-GMsFEM Algorithm 2 iterated from the exact solution u_k to Eq. (11). By the definition, $\tilde{u}_{k+1}^{\text{cem}} = \mathcal{S}\{b(u_k), \kappa, f, p\}$ and $u_{k+1}^{\text{cem}} = \mathcal{S}\{b(u_k^{\text{cem}}), \kappa, f, p\}$. Because u_k and u_k^{cem} belong to $\mathcal{B}_{r_0}(u_*)$, we have

$$\|\tilde{u}_{k+1}^{\text{cem}} - u_{k+1}^{\text{cem}}\|_a \leq C_* \|u_k - u_k^{\text{cem}}\|_a \quad (24)$$

by the Assumption 5.3. We can split $\|u_{k+1} - u_{k+1}^{\text{cem}}\|_a$ by introducing $\tilde{u}_{k+1}^{\text{cem}}$:

$$\begin{aligned} \|u_{k+1} - u_{k+1}^{\text{cem}}\|_a &= \|u_{k+1} - \tilde{u}_{k+1}^{\text{cem}} + \tilde{u}_{k+1}^{\text{cem}} - u_{k+1}^{\text{cem}}\|_a, \\ &\leq \|u_{k+1} - \tilde{u}_{k+1}^{\text{cem}}\|_a + \|\tilde{u}_{k+1}^{\text{cem}} - u_{k+1}^{\text{cem}}\|_a. \end{aligned}$$

For simplicity, we take $e_k = u_k - u_k^{\text{cem}}$, which implies $e_0 = 0$. From Lemma 5.2 and Assumption 5.3, it follows that

$$\|e_{k+1}\|_a \leq C'H (\|f\|_{L^2} + \|p\|_{L^2(\Gamma_N)}) + C_* \|e_k\|_a. \quad (25)$$

Dividing Eq. (25) on both sides by C_*^{k+1} , we have

$$\frac{\|e_{k+1}\|_a}{C_*^{k+1}} \leq \frac{C'H}{C_*^{k+1}} (\|f\|_{L^2} + \|p\|_{L^2(\Gamma_N)}) + \frac{\|e_k\|_a}{C_*^k}.$$

Since u_i and u_i^{cem} belong to $\mathcal{B}_{r_0}(u_*) \subset V$ for all $0 \leq i \leq k$, we have

$$\frac{\|e_{i+1}\|_a}{C_*^{i+1}} - \frac{\|e_i\|_a}{C_*^i} \leq \frac{C'H}{C_*^{i+1}} (\|f\|_{L^2} + \|p\|_{L^2(\Gamma_N)}), \quad \forall 0 \leq i \leq k.$$

We can sum the left-hand term for $0 \leq i \leq k$ and build the inequality as follows:

$$\begin{aligned} \frac{\|e_{k+1}\|_a}{C_*^{k+1}} &= \sum_{i=0}^k \left(\frac{\|e_{i+1}\|_a}{C_*^{i+1}} - \frac{\|e_i\|_a}{C_*^i} \right) \\ &\leq C'H \sum_{i=0}^k \frac{1}{C_*^{i+1}} (\|f\|_{L^2} + \|p\|_{L^2(\Gamma_N)}), \\ &= C'H \frac{C_*^{k+1} - 1}{C_*^{k+2} - C_*^{k+1}} (\|f\|_{L^2} + \|p\|_{L^2(\Gamma_N)}). \end{aligned}$$

As a result, we obtain

$$\|e_{k+1}\|_a \leq C'H \frac{C_*^{k+1} - 1}{C_* - 1} (\|f\|_{L^2} + \|p\|_{L^2(\Gamma_N)}).$$

Since $C_* = 1 + \delta$ with $0 < \delta < 1$ and δ small enough, then

$$\|e_{k+1}\|_a \leq C'H \frac{(1 + \delta)^{k+1} - 1}{(1 + \delta) - 1} (\|f\|_{L^2} + \|p\|_{L^2(\Gamma_N)}).$$

Choosing a suitable constant M such that

$$\frac{(1 + \delta)^{k+1} - 1}{(1 + \delta) - 1} \leq M,$$

we have

$$\|e_{k+1}\|_a \leq C'MH (\|f\|_{L^2} + \|p\|_{L^2(\Gamma_N)}),$$

for all $k \leq k_0$, where

$$k_0 = \left\lfloor \frac{\log(\delta M + 1)}{\log(1 + \delta)} - 1 \right\rfloor.$$

From the Theorem 5.1, u_k converges superlinearly to u_* , without loss of generality, assume $\|u_* - u_k\|_a < 2^{-k} r$ for all $k \geq 0$. We can split $\|u_* - u_{k+1}^{\text{cem}}\|_a$ and derive the following error estimates,

$$\begin{aligned} \|u_* - u_{k+1}^{\text{cem}}\|_a &\leq \|u_* - u_{k+1}\|_a + \|u_{k+1} - u_{k+1}^{\text{cem}}\|_a, \\ &\leq \|u_* - u_{k+1}\|_a + C'MH (\|f\|_{L^2} + \|p\|_{L^2(\Gamma_N)}), \\ &< 2^{-(k+1)} r + C'MH (\|f\|_{L^2} + \|p\|_{L^2(\Gamma_N)}), \end{aligned}$$

□

Indeed, if we choose appropriate initial u_0 and u_0^{cem} , and make H sufficiently small, we can effectively control the error between the numerical solution and the exact solution at each iteration. We can also enhance the accuracy and convergence of the algorithm.

6. Conclusion

The paper presents a new iterative multiscale method based on the CEM-GMsFEM for solving the contact problem of Signorini type. This mixed contact boundary problem can be converted to a nonlinear unconstrained minimizing problem by applying the penalty method. The semismooth Newton method can be introduced to handle the challenges raised by the nonlinear and non-smooth contact conditions. Note that the variational form of an inhomogeneous Robin boundary value problem happen to be the same as that in semismooth Newton iteration. So the CEM-GMsFEM is employed iteratively to construct multiscale basis functions, which can effectively capture the solution behavior near the contact boundary. Numerical experiments were conducted using various heterogeneous coefficient profiles and tested with different initial conditions and parameters. The results validate our method holds particular significance in effectively addressing the challenges posed by non-linearity encountered in contact problems. The analysis demonstrates the proposed method is capable of providing accurate numerical solutions with fast convergence rates.

In future research, we plan to investigate the scalability and performance of large-scale problems by our method. Additionally, according to our experience, the construction of multiscale basis functions can be time-consuming. Therefore, it would be valuable to explore parallel computing approaches to speed up this process, which are rare in previous studies. Moreover, another interesting research direction is to extend our method to handle more realistic problems, such as dynamic contact and impact contact with friction.

Acknowledgment

The research of Eric Chung is partially supported by the Hong Kong RGC General Research Fund (Project: 14305222).

References

- [1] Z. Chen, T. Y. Hou, A mixed multiscale finite element method for elliptic problems with oscillating coefficients, *Mathematics of Computation* 72 (242) (2003) 541–576. doi:<http://dx.doi.org/10.1090/S0025-5718-02-01441-2>.
- [2] Y. Efendiev, T. Y. Hou, *Multiscale finite element methods: theory and applications*, Vol. 4, Springer Science & Business Media, 2009. doi:<http://dx.doi.org/10.1007/978-0-387-09496-0>.
- [3] T. Y. Hou, X. Wu, A multiscale finite element method for elliptic problems in composite materials and porous media, *Journal of Computational Physics* 134 (1997) 169–189. doi:10.1006/jcph.1997.5682. URL <https://www.sciencedirect.com/science/article/pii/S0021999197956825>
- [4] T. Y. Hou, X. Wu, Z. Cai, Convergence of a multiscale finite element method for elliptic problems with rapidly oscillating coefficients, *Mathematics of computation* 68 (227) (1999) 913–943. doi:<http://dx.doi.org/10.1090/S0025-5718-99-01077-7>.
- [5] A. Abdulle, W. E. B. Engquist, E. Vanden-Eijnden, The heterogeneous multiscale method, *Acta Numerica* 21 (2012) 1–87. doi:<http://dx.doi.org/10.1017/S0962492912000025>.
- [6] P. Ming, P. Zhang, Analysis of the heterogeneous multiscale method for elliptic homogenization problems, *Journal of the American Mathematical Society* 18 (1) (2005) 121–156. doi:<http://dx.doi.org/10.1090/S0894-0347-04-00469-2>.

- [7] W. E. B. Engquist, X. Li, W. Ren, E. Vanden-Eijnden, Heterogeneous multiscale methods: a review, *Communications in computational physics* 2 (3) (2007) 367–450.
- [8] T. J. R. Hughes, Multiscale phenomena: Green’s functions, the Dirichlet-to-Neumann formulation, subgrid scale models, bubbles and the origins of stabilized methods, *Computer methods in applied mechanics and engineering* 127 (1-4) (1995) 387–401. doi:[http://dx.doi.org/10.1016/0045-7825\(95\)00844-9](http://dx.doi.org/10.1016/0045-7825(95)00844-9).
- [9] T. J. R. Hughes, G. Sangalli, Variational multiscale analysis: the fine-scale Green’s function, projection, optimization, localization, and stabilized methods, *SIAM Journal on Numerical Analysis* 45 (2) (2007) 539–557. doi:<http://dx.doi.org/10.1137/050645646>.
- [10] I. Babuška, R. Lipton, P. Sinz, M. Stuebner, Multiscale-spectral GFEM and optimal oversampling, *Computer Methods in Applied Mechanics and Engineering* 364 (2020) 112960. doi:<http://dx.doi.org/10.1016/j.cma.2020.112960>.
- [11] I. Babuška, R. Lipton, Optimal local approximation spaces for generalized finite element methods with application to multiscale problems, *Multiscale Modeling & Simulation* 9 (1) (2011) 373–406. doi:<http://dx.doi.org/10.1137/100791051>.
- [12] Y. Efendiev, J. Galvis, T. Y. Hou, Generalized multiscale finite element methods (GMsFEM), *Journal of computational physics* 251 (2013) 116–135. doi:<http://dx.doi.org/10.1016/j.jcp.2013.04.045>.
- [13] E. T. Chung, Y. Efendiev, W. T. Leung, Generalized multiscale finite element methods for wave propagation in heterogeneous media, *Multiscale Modeling & Simulation* 12 (4) (2014) 1691–1721. doi:<https://doi.org/10.1137/130926675>.
- [14] E. T. Chung, Y. Efendiev, T. Y. Hou, Adaptive multiscale model reduction with generalized multiscale finite element methods, *Journal of Computational Physics* 320 (2016) 69–95. doi:<https://doi.org/10.1016/j.jcp.2016.04.054>.
- [15] F. Hellman, A. Målqvist, Contrast independent localization of multiscale problems, *Multiscale Modeling & Simulation* 15 (4) (2017) 1325–1355. doi:<http://dx.doi.org/10.1137/16M1100460>.
- [16] P. Henning, A. Målqvist, Localized orthogonal decomposition techniques for boundary value problems, *SIAM Journal on Scientific Computing* 36 (4) (2014) A1609–A1634. doi:[10.1137/130933198](https://doi.org/10.1137/130933198).
- [17] A. Målqvist, D. Peterseim, Localization of elliptic multiscale problems, *Mathematics of Computation* 83 (290) (2014) 2583–2603. doi:<http://dx.doi.org/10.1090/S0025-5718-2014-02868-8>.
- [18] A. Målqvist, D. Peterseim, Numerical homogenization by localized orthogonal decomposition, *SIAM*, 2020. doi:<http://dx.doi.org/10.1137/1.9781611976458>.
- [19] A. Signorini, Questioni di elasticità non linearizzata e semilinearizzata, *Rend. Mat. Appl* 18 (5) (1959) 95–139.
- [20] G. Fichera, Problemi elastostatici con vincoli unilaterali: il problema di Signorini con ambigue condizioni al contorno, *Accademia nazionale dei Lincei*, 1964.
- [21] J. L. Lions, G. Stampacchia, Variational inequalities, *Communications on Pure and Applied Mathematics* 20 (3) (1967) 493–519. doi:<https://doi.org/10.1002/cpa.3160200302>.
URL <https://onlinelibrary.wiley.com/doi/abs/10.1002/cpa.3160200302>
- [22] G. Rozza, D. B. P. Huynh, A. T. Patera, Reduced basis approximation and a posteriori error estimation for affinely parametrized elliptic coercive partial differential equations: application to transport and continuum mechanics, *Archives of Computational Methods in Engineering* 15 (3) (2008) 229–275. doi:<http://dx.doi.org/10.1007/s11831-008-9019-9>.
- [23] B. Haasdonk, J. Salomon, B. Wohlmuth, A reduced basis method for parametrized variational inequalities, *SIAM Journal on Numerical Analysis* 50 (5) (2012) 2656–2676. doi:[10.1137/110835372](https://doi.org/10.1137/110835372).
URL <https://doi.org/10.1137/110835372>
- [24] J. Fauque, I. Ramière, D. Ryckelynck, Hybrid hyper-reduced modeling for contact mechanics problems, *International Journal for Numerical Methods in Engineering* 115 (1) (2018) 117–139. doi:<http://dx.doi.org/10.1002/nme.5798>.
- [25] J. Krciszek, R. Pinnau, Model reduction of contact problems in elasticity: proper orthogonal decomposition for variational inequalities, in: *Progress in Industrial Mathematics at ECMI 2012*, Springer, 2014, pp. 277–284. doi:http://dx.doi.org/10.1007/978-3-319-05365-3_38.
- [26] N. Kikuchi, J. T. Oden, Contact problems in elasticity: a study of variational inequalities and finite element methods, *SIAM*, 1988.
- [27] J. Haslinger, I. Hlaváček, Contact between elastic bodies. ii. finite element analysis, *Aplikace Matematiky* 26 (4) (1981) 263–290.
- [28] D. Kinderlehrer, G. Stampacchia, An introduction to variational inequalities and their applications, *SIAM*, 2000. doi:<http://dx.doi.org/10.1137/1.9780898719451>.
- [29] J. Haslinger, I. Hlaváček, J. Nečas, Numerical methods for unilateral problems in solid mechanics, in: *Finite Element Methods (Part 2), Numerical Methods for Solids (Part 2)*, Vol. 4 of *Handbook of Numerical Analysis*, Elsevier, 1996, pp. 313–485. doi:[https://doi.org/10.1016/S1570-8659\(96\)80005-6](https://doi.org/10.1016/S1570-8659(96)80005-6).
URL <https://www.sciencedirect.com/science/article/pii/S1570865996800056>

- [30] F. Ben Belgacem, Y. Renard, Hybrid finite element methods for the Signorini problem, *Mathematics of Computation* 72 (2003) 1117–1145. doi:10.1090/S0025-5718-03-01490-X.
- [31] X. Su, S. M. Pun, A multiscale method for the heterogeneous Signorini problem, *Journal of Computational and Applied Mathematics* 409 (2022) 114160. doi:10.1016/j.cam.2022.114160.
URL <https://www.sciencedirect.com/science/article/pii/S0377042722000449>
- [32] P. Wriggers, T. A. Laursen, *Computational contact mechanics*, Vol. 2, Springer, 2006. doi:<http://dx.doi.org/10.1007/978-3-540-32609-0>.
- [33] M. Hintermüller, *Semismooth Newton methods and applications*, Department of Mathematics, Humboldt-University of Berlin (2010).
- [34] E. T. Chung, Y. Efendiev, W. T. Leung, Constraint energy minimizing generalized multiscale finite element method, *Computer Methods in Applied Mechanics and Engineering* 339 (2018) 298–319. doi:10.1016/j.cma.2018.04.010.
URL <https://www.sciencedirect.com/science/article/pii/S0045782518301804>
- [35] C. Ye, E. T. Chung, Constraint energy minimizing generalized multiscale finite element method for inhomogeneous boundary value problems with high contrast coefficients, *Multiscale Modeling & Simulation* 21 (1) (2023) 194–217, publisher: Society for Industrial and Applied Mathematics. doi:10.1137/21M1459113.
URL <https://epubs.siam.org/doi/abs/10.1137/21M1459113>